Facile Bottom-up Preparation of WS$_2$-Based Water-Soluble Quantum Dots as Luminescent Probes for Hydrogen Peroxide and Glucose

Da-Ren Hang[1,2*] (iD), De-You Sun[1], Chun-Hu Chen[3], Hui-Fen Wu[3], Mitch M. C. Chou[1,2], Sk Emdadul Islam[1] and Krishna Hari Sharma[1]

Abstract

Photoluminescent zero-dimensional (0D) quantum dots (QDs) derived from transition metal dichalcogenides, particularly molybdenum disulfide, are presently in the spotlight for their advantageous characteristics for optoelectronics, imaging, and sensors. Nevertheless, up to now, little work has been done to synthesize and explore photoluminescent 0D WS$_2$ QDs, especially by a bottom-up strategy without using usual toxic organic solvents. In this work, we report a facile bottom-up strategy to synthesize high-quality water-soluble tungsten disulfide (WS$_2$) QDs through hydrothermal reaction by using sodium tungstate dihydrate and L-cysteine as W and S sources. Besides, hybrid carbon quantum dots/WS$_2$ QDs were further prepared based on this method. Physicochemical and structural analysis of QD hybrid indicated that the graphitic carbon quantum dots with diameters about 5 nm were held onto WS$_2$ QDs via electrostatic attraction forces. The resultant QDs show good water solubility and stable photoluminescence (PL). The excitation-dependent PL can be attributed to the polydispersity of the synthesized QDs. We found that the PL was stable under continuous irradiation of UV light but can be quenched in the presence of hydrogen peroxide (H$_2$O$_2$). The obtained WS$_2$-based QDs were thus adopted as an electrodeless luminescent probe for H$_2$O$_2$ and for enzymatic sensing of glucose. The hybrid QDs were shown to have a more sensitive LOD in the case of glucose sensing. The Raman study implied that H$_2$O$_2$ causes the partial oxidation of QDs, which may lead to oxidation-induced quenching. Overall, the presented strategy provides a general guideline for facile and low-cost synthesis of other water-soluble layered material QDs and relevant hybrids in large quantity. These WS$_2$-based high-quality water-soluble QDs should be promising for a wide range of applications in optoelectronics, environmental monitoring, medical imaging, and photocatalysis.

Keywords: Semiconductors, Quantum localization, Chemical synthesis, Luminescence, Optical properties

Introduction

In the past decade, graphene has opened a new horizon of two-dimensional (2D) materials for chemists and physicists [1–3]. Due to the inherent shortcomings of graphene, such as absence of band gap, research for other kinds of 2D materials is currently in the spotlight. Notable 2D material groups include layered transition metal dichalcogenides (TMDs), layered transition metal oxides, and carbide-based materials [4–8]. The characteristic 2D structure of TMD results in anisotropic physical properties, ranging from electron mobility to catalytic and optical properties. In comparison with their bulk counterpart, the general advantages of ultra-thin TMDs are the tunable physical properties and the enriched active sites for chemical reactions. As the most popular 2D TMD material, single-layer or multilayer

* Correspondence: drhang@faculty.nsysu.edu.tw
[1]Department of Materials and Optoelectronic Science, National Sun Yat-sen University, Kaohsiung 80424, Taiwan
[2]Center of Crystal Research, National Sun Yat-sen University, Kaohsiung 80424, Taiwan
Full list of author information is available at the end of the article

molybdenum disulfide (MoS_2) has shown great potential in a wide range of applications, such as electronics, sensors, and photocatalysis [9–11]. Especially, ultrathin atomic-layered MoS_2 holds great promise for constructing biosensors because high specific surface area and ample active surface states make 2D MoS_2 very sensitive to exposure to target analytes. In the field of biosensing, 2D MoS_2 has a relatively low toxicity in comparison to many other nanomaterials, in particular, graphene and graphene oxides [12]. For instance, 2D MoS_2 has been employed for the detection of hydrogen peroxide (H_2O_2) and glucose in the last couple of years [13–15].

The detection of hydrogen peroxide, a vital reactive oxygen species, is of practical importance in chemical, pharmaceutical, clinical, and environmental fields. For example, an abnormal high level of H_2O_2 could mean the generation of acid rain and could indicate the risk of a few diseases like Alzheimer's disease and Parkinson's disease [16]. On the other hand, glucose plays an important role in biochemical pathway and human health evaluation. Convenient and cheap detection of glucose is of considerable significance in the diabetes mellitus diagnosis, food, and biofuel cell analysis. Besides, it is known that over 80% of biosensor industry research is related to glucose sensors. Therefore, the development of a facile, low-priced, and accurate sensor for H_2O_2 and glucose continue to receive tremendous research effort [17, 18].
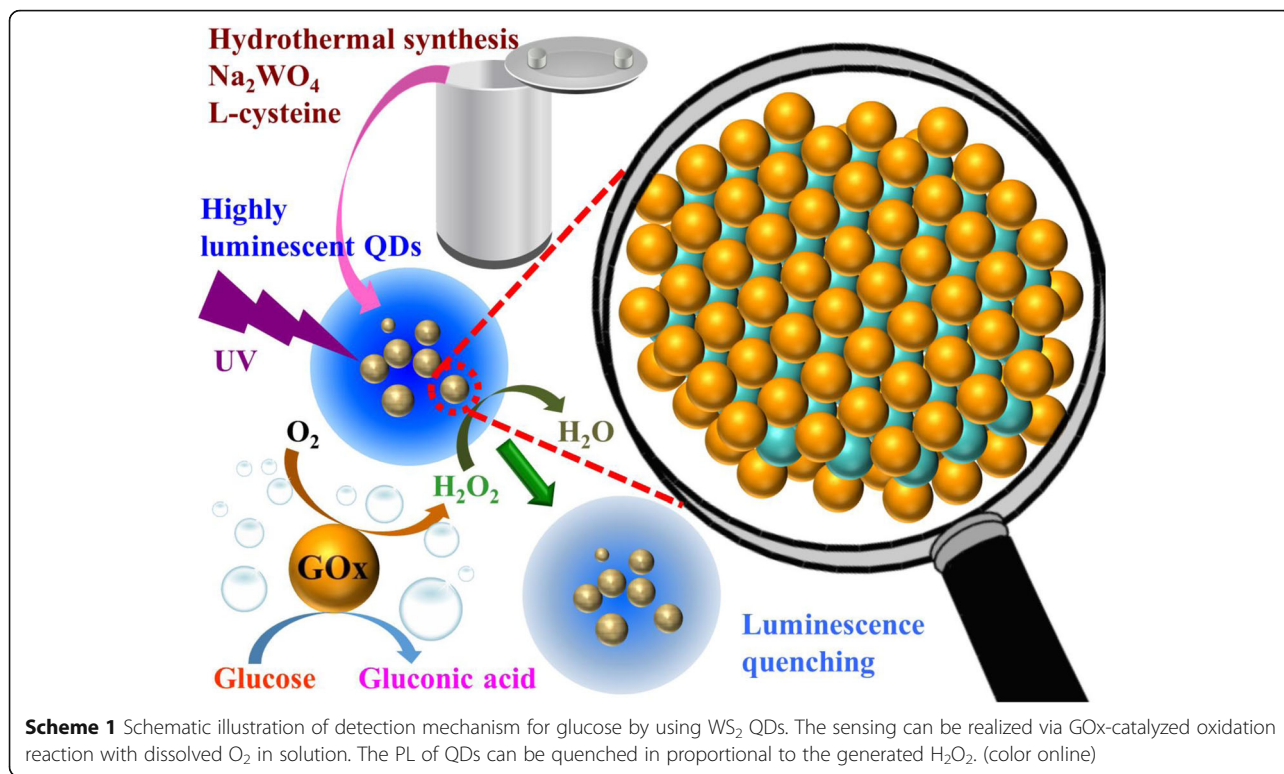
Zero-dimensional (0D) quantum dots (QDs) derived from ultrathin 2D materials are emerging as a novel category of nanoscale 0D materials [19, 20]. Compared with TMD nanosheets, TMD QDs show distinct and exceptional physical properties due to pronounced quantum confinement and edge effects. By reducing the dimensions of QDs close to the excitonic Bohr radius, it was found that the quantum confinement effect (QCE) enhanced the photoluminescence (PL) quantum efficiency of MoS_2 QDs [21, 22]. Moreover, the ultrathin sizes of MoS_2 QDs lead to larger surface-to-volume ratio and abundant active edge states, making them chemically sensitive to the surroundings. Thus TMD QDs can be promising for use in sensing, luminescence, bioimaging, and catalysis. In this regard, MoS_2 QDs were lately employed for PL sensor to detect chemical and bioanalyte [23, 24].

Following the successful development of MoS_2 in various applications, tungsten disulfide (WS_2) begins to receive increasing amount of attention [25]. The layer structure consists of 2D monolayer building blocks held by weak van der Waals interaction. Each WS_2 single layer possesses a hexagonal crystal structure formed by covalently bonded S-W-S monolayers, where a tungsten atom sheet is sandwiched by two layers of S atoms. Compared with molybdenum, tungsten has several benefits such as copious natural resources, cheaper prices,

and less toxicity, which is favorable for industrial applications. Additionally, the larger size of W provides more spacious interlayer channels in the 2D structure and facilitates physical property modulation via substitutional doping. WS_2 is also preferential in tungsten dichalcogenides when a high chemical reactivity is in need at the unsaturated sulfur edges. 2D WS_2 nanosheets have recently found a number of applications, such as FETs [26], photodetectors [27, 28], and photocatalysis [29, 30]. WS_2 in its bulk form has an indirect bandgap and a photoluminescence (PL) band in infrared with low quantum efficiency [25]. In QD configuration, 0D WS_2 has a direct bandgap and hence shows highly efficient PL, facilitating the construction of electrodeless optical sensing templates. The resultant PL that appears in the visible range is compatible with most low-cost commercial optical platforms. Advantageously, the noncontact nature of optical sensing supports the future realization of advanced integrated multifunctional microchips.
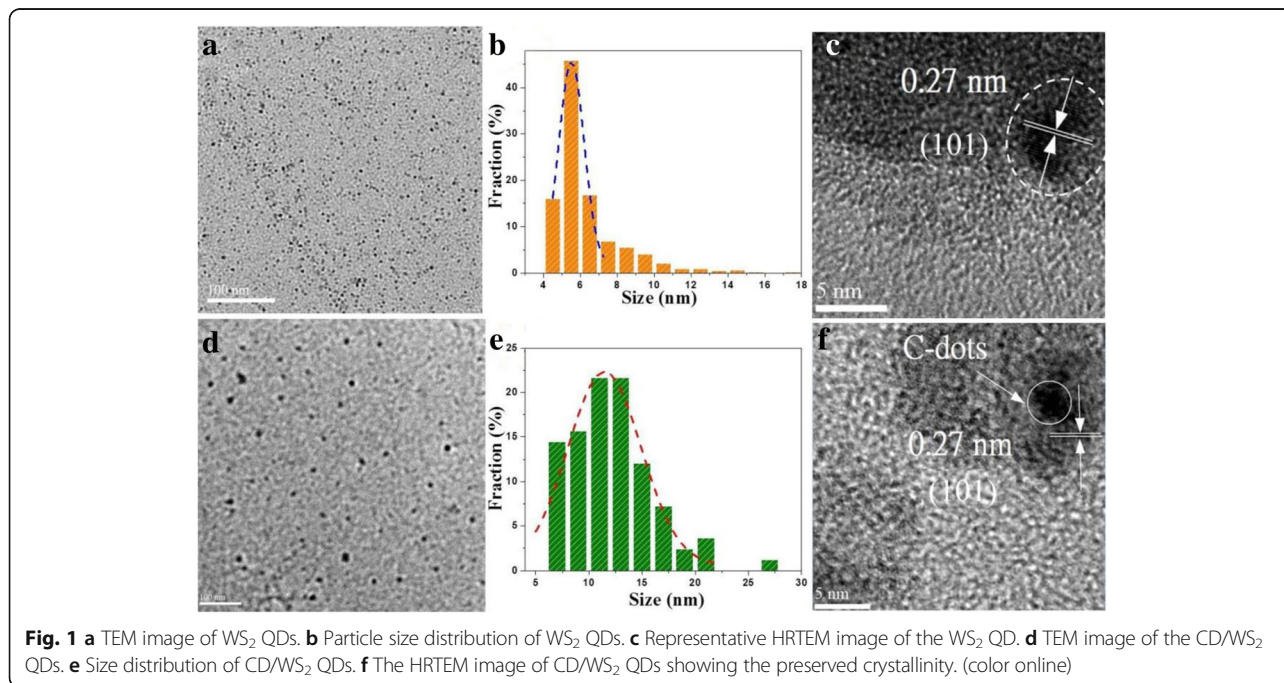
To date, considerable efforts have been dedicated to achieve the synthesis of photoluminescent MoS_2 QD materials [22, 31]. In contrast, the progress in the synthesis and application of photoluminescent WS_2 QDs is still rather limited. In general, synthetic strategies can be divided into "top-down" and "bottom-up" approaches. As for the "top-down" methods, liquid exfoliation methods are usually regarded as an efficient methodology to prepare single or few-layered 2D material suspensions in large quantities. Successful preparations of WS_2 QDs by intercalation techniques adopting lithium and K ions have been reported [32, 33]. In such cases, hazardous and time-consuming processes were involved. Besides, further purification was required to remove ionic residues and semiconducting properties could be weakened because of ion intercalation. On the other hand, sonication-assisted liquid-phase exfoliation technique is based on high ultrasonic powers and the match of surface tension between the solvents and the targeted stratified bulk materials [34–36]. Several recent reports on the preparation of WS_2 QDs have employed this rather universal route [37–40]. However, this technique is usually associated with hazardous organic solvents and laborious pretreatment, and is quite sensitive to the environmental conditions. In addition, the derived product is typically plagued with residue solvents. The high-temperature posttreatment process is thus required to get rid of excessive solvents with high boiling points. Nevertheless, it may lead to the aggregation of WS_2 QDs and the formation of harmful side products in certain cases.
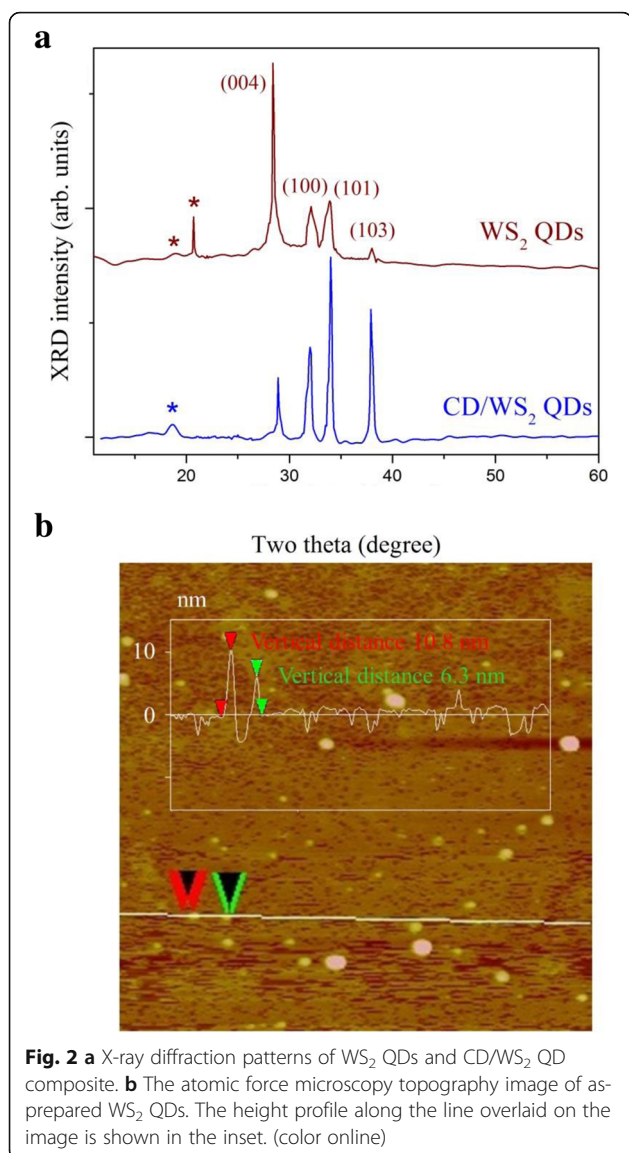
While most of these synthetic routes belong to "top-down" synthesis, the advancement in the "bottom-up" synthesis of photoluminescent WS_2 QDs is fairly restricted [41, 42]. Among the "bottom-up" chemical synthetic approaches, the hydrothermal method has become a well-received and cost-effective technique for

Hang *et al. Nanoscale Research Letters*   (2019) 14:271

Page 3 of 15

Scheme 1 Schematic illustration of detection mechanism for glucose by using WS$_2$ QDs. The sensing can be realized via GOx-catalyzed oxidation reaction with dissolved O$_2$ in solution. The PL of QDs can be quenched in proportional to the generated H$_2$O$_2$. (color online)

preparing semiconducting nanocrystals. The dimension and morphology of the synthesized nanostructures can be easily controlled by the chemical reaction parameters and precursor selection. In comparison with most "top-down" synthesis, the hydrothermal process is simple, environmentally benign, and well-suited to the facile formation of nanohybrid materials. Moreover, a recent investigation on hydrothermally prepared MoS$_2$ QDs suggested that the solubility and stability of MoS$_2$ QDs were improved due to some accompanying surface functional groups [24]. Due to these favorable attributes, the exploration of facile hydrothermal synthesis of water-

Fig. 1 a TEM image of WS$_2$ QDs. **b** Particle size distribution of WS$_2$ QDs. **c** Representative HRTEM image of the WS$_2$ QD. **d** TEM image of the CD/WS$_2$ QDs. **e** Size distribution of CD/WS$_2$ QDs. **f** The HRTEM image of CD/WS$_2$ QDs showing the preserved crystallinity. (color online)

Hang *et al. Nanoscale Research Letters* (2019) 14:271

Page 4 of 15

Fig. 2 a X-ray diffraction patterns of WS_2 QDs and CD/WS_2 QD composite. **b** The atomic force microscopy topography image of as-prepared WS_2 QDs. The height profile along the line overlaid on the image is shown in the inset. (color online)

dispersible WS_2 QDs with stable photoluminescence is significant and urgent at this stage. In this paper, we herein present a facile bottom-up hydrothermal route for the synthesis of photoluminescent WS_2 QDs. Furthermore, motivated by recent progress in carbon quantum dots (CDs)/2D MoS_2 composites and to show the viable hybrid formation by hydrothermal protocol, we proceeded to prepare CD/WS_2 QDs for the first time [43–45]. CDs are 0D quasi-spherical nanoparticles, with diameter in the order of 10 nm or less, showing superb solubility, biocompatibility, photochemical stability, and rapid electron transfer properties [46]. Next, the prepared WS_2 QDs were characterized in detail. The intense blue emission from synthesized QDs was then used as luminescent probes to construct electrodeless PL sensors for detection of hydrogen peroxide and glucose. Likewise, the sensors displayed a good selectivity

toward glucose over other probable interfering species. In the case of glucose sensing, it was found that the hybrid CD/WS_2 QDs have a more sensitive LOD than that of pristine WS_2 QDs. The obtained results indicated that the synthesized WS_2 QDs and novel CD/WS_2 hybrid QDs possess small sizes, stable and intense PL, high dispersibility, and non-toxicity. We believe that these optical active WS_2 QDs are promising to serve as new platforms for chemical and biological molecules sensors and other functional devices. Extended studies toward this direction are currently ongoing.

Methods
Reagents and Chemicals
Sodium tungstate dihydrate ($Na_2WO_4 \cdot 2H_2O$) was obtained from Nihon Shiyaku Reagent (Tokyo, Japan). L-cysteine was purchased from Alfa Aesar. They served as starting materials for the hydrothermal synthesis of WS_2 QDs. Here, L-cysteine acts as sulfur source as well as reducing agent. Glucose, fructose, maltose, and sucrose were obtained from Honeywell Fluka (Shanghai, China). Lactose, histidine, glycine, potassium chloride, and magnesium chloride were obtained from Sigma-Aldrich. All the reagents were of analytical purity and were used as received without further purification. Throughout the synthesis, ultra-pure water from Milli-Q Plus water purification system (Millipore Co., Bedford, MA, USA) was adopted for solution preparation.
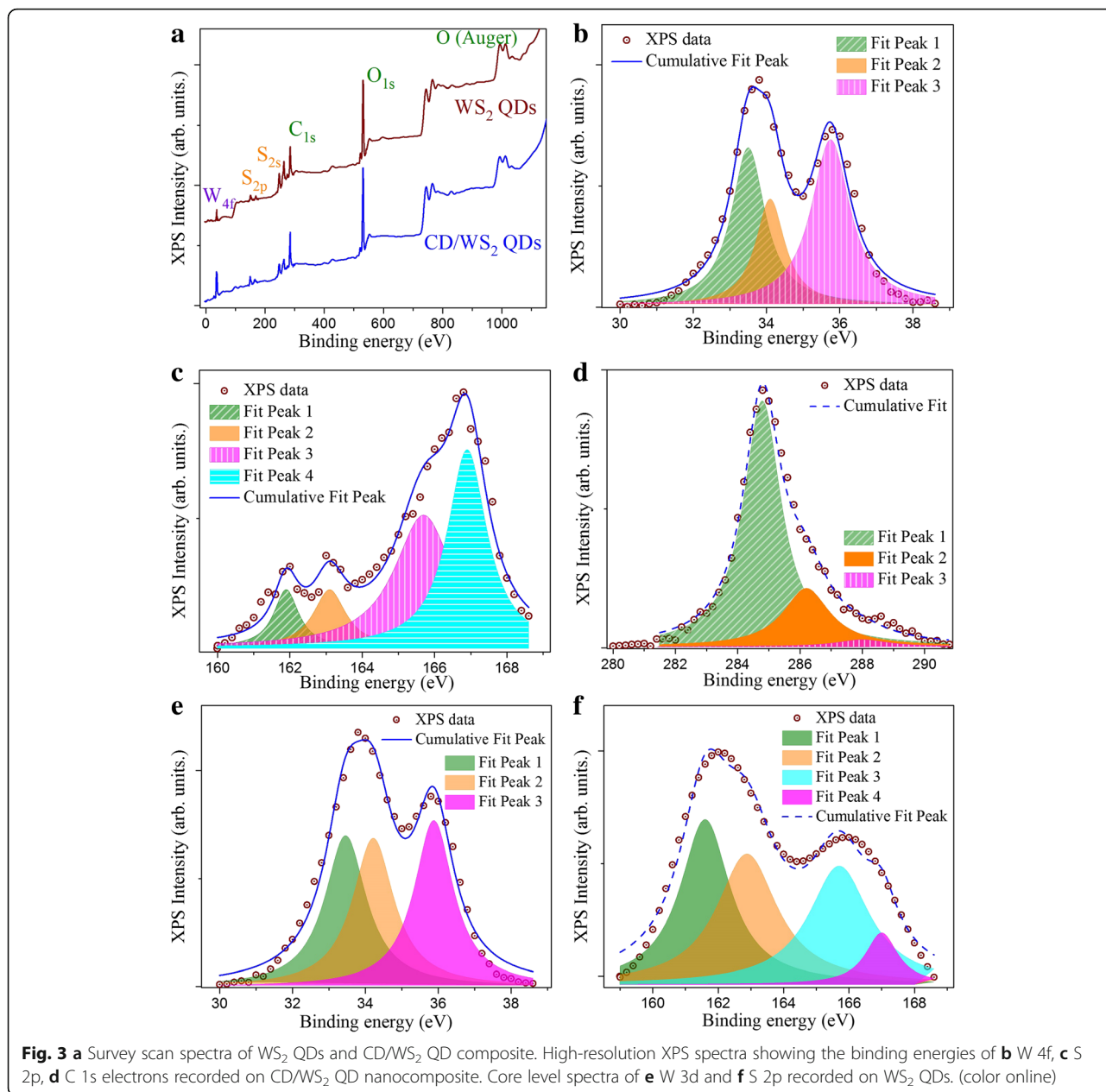
Materials Preparation
Synthesis of 0D WS_2 QDs
The water-soluble WS_2 QDs were synthesized through a facile and one-step hydrothermal method. The synthetic procedure is concisely shown in Scheme 1. In short, 0.066 g of $Na_2WO_4 \cdot 2H_2O$ was dissolved in 12.5 mL of ultrapure water with further ultrasonication for 5 min. Then 0.1 M HCl was added to adjust the pH to 6.5. Afterward, 0.0242 g of L-cysteine and 50 mL of water were poured into the solution and was followed by ultrasonication for 10 min. The mixture was subsequently transferred into a 100-mL Teflon-lined stainless steel autoclave and reacted at 180 °C for 24 h. After the autoclave cooled naturally, the supernatant containing WS_2 QDs was centrifuged for 20 min at the speed of 10,000 rpm. The WS_2 QD product was collected and then stored in a refrigerator at 4 °C.

Synthesis of Carbon Quantum Dots
Carbon quantum dots were prepared by an eco-friendly microwave-assisted method, which is analogous to the CD synthesis in previous reports [47, 48]. In a typical

Hang *et al. Nanoscale Research Letters* (2019) 14:271

Page 5 of 15

Fig. 3 **a** Survey scan spectra of WS_2 QDs and CD/WS_2 QD composite. High-resolution XPS spectra showing the binding energies of **b** W 4f, **c** S 2p, **d** C 1s electrons recorded on CD/WS_2 QD nanocomposite. Core level spectra of **e** W 3d and **f** S 2p recorded on WS_2 QDs. (color online)

production, 17.1 g of sucrose was dissolved in deionized water to prepare 1 M sucrose solution. Next, the solution was subjected to microwave heating at 500 W for 20 min. The CD can be collected and filtered through a filter. After that, the CD solution was stored at 4 °C for further experiments.

Synthesis of CD/WS_2 QDs

For synthesis of hybrid CD/WS_2 QDs, certain amounts of CD solutions were sonicated for 20 min to achieve uniform dispersion. The CD solution was added to the preceding WS_2 precursor solution with vigorous stirring for 15 min. Next, the homogeneous mixture was

transferred into a 100-mL Teflon-lined autoclave and kept at 180 °C for 24 h. After the suspension was cooled to room temperature, the CD/WS_2 QDs were collected by using centrifugation for 20 min at 10,000 rpm.

Material Characterization

The phase structure was characterized by a Siemens D5000 powder diffractometer utilizing $Cu_{K\alpha}$ radiation (λ = 1.5418 Å). Further microstructural information of the samples was provided by transmission electron microscopy (TEM) and high-resolution transmission electron microscopy (HRTEM) by using a JEOL-3010 transmission electron microscope. X-ray photoelectron
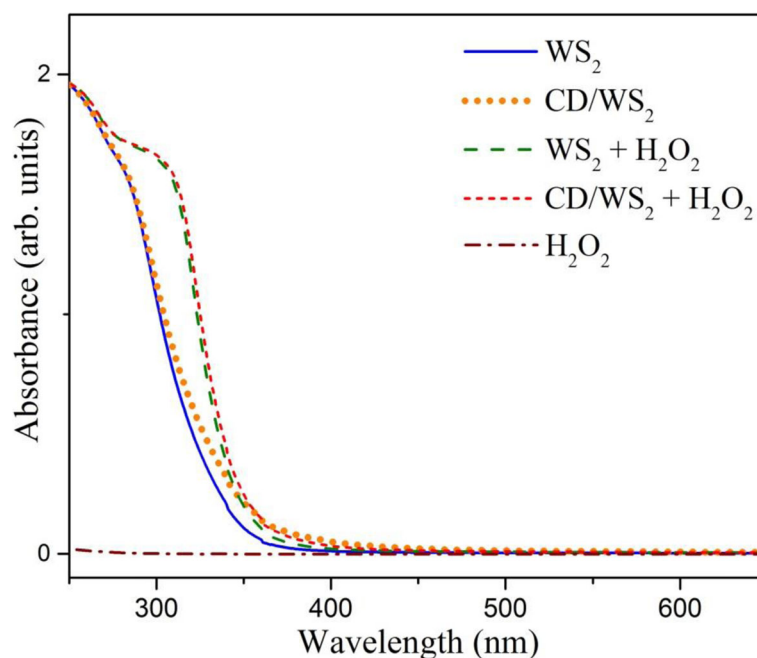
Fig. 4 UV–Vis absorption spectra of WS$_2$ QDs (blue line) and CD/WS$_2$ QDs (orange dot line). UV–Vis spectra of WS$_2$ QDs and CD/WS$_2$ QDs in the presence of H$_2$O$_2$ are plotted as green dashed line and red dashed line, respectively. The brown dashed dot line shows the absorbance for H$_2$O$_2$ alone. (color online)

spectroscopy (XPS) measurements were carried out with an ultrahigh vacuum JEOL JPS-9010 electron spectrometer equipped with a multi-channel detector. The collected binding energies were referenced to the C1s peaks at 284.6 eV of the surface adventitious carbon. The UV–Vis spectra were recorded with a Jasco V-630 spectrophotometer (USA) with a standard 10-mm path length quartz cuvette. The photoluminescence (PL) and photoluminescence excitation (PLE) spectra of the as-prepared samples were measured using a Hitachi F-4500 florescence spectrophotometer linked to a 150 W Xenon lamp as the excitation source. The PL decay time of the QDs was recorded on an Edinburgh Instruments OB920 Fluorescence Lifetime Spectrometer (Edinburgh Instruments Ltd., Livingston, UK). The Raman measurements were taken in ambient conditions with a red light laser. The scattered light was collected by the same objective lens and dispersed with a Horiba iHR320 spectrometer [49].

Results and Discussion
Structural and Morphological Studies
The facile one-pot hydrothermal process to prepare water-dispersible WS$_2$ QDs is tersely illustrated in Scheme 1. The preparation details are described in the experimental section. The structural information of the as-formed WS$_2$ QDs was firstly investigated by transmission electron microscopy (TEM) and high-resolution transmission

electron microscopy (HRTEM), as shown in Fig. 1. A typical TEM image of the resultant WS$_2$ QDs (Fig. 1a) shows that the QDs are uniformly dispersed in aqueous phase without apparent aggregation. The excellent water solubility can be derived by residual hydrophilic amino or carboxyl groups on the synthesized QD surface. The lateral size distribution of QDs is shown by plotting the histogram in Fig. 1b, where up to 76% QDs are distributed in the narrow range from 4 to 7 nm. The HRTEM image in Fig. 1c reveals that the lattice fringe spacing of the WS$_2$ QD was 0.27 nm, which is matched with the (101) plane of hexagonal WS$_2$ crystal [37, 50]. Figure 1d shows the TEM image of the as-prepared hybrid CD/WS$_2$ QDs with good dispersion. The statistical analysis of particle size distribution was conducted and presented in Fig. 1e. It can be found that the average particle size of hybrid QDs is 11.5 nm and the majority lies in the range of 7–15 nm. Figure 1f presents a typical HRTEM image of one of the hybrid QD in which CDs can be found on the QD surface. In addition, the (101) d-spacing of 2H-WS$_2$ was once again observed in the hybrid QD as with the pristine QD material, implying that the good crystalline structure was retained after the hybrid formation.

X-ray diffraction (XRD) was employed to further examine the crystal structures of WS$_2$ QDs and CD/WS$_2$ QDs. The XRD patterns obtained are displayed in Fig. 2a, the diffraction peaks at 2θ = 28.9°, 32°, 33.9°, and 38.0° correspond to (004), (100), (101), and (103) lattice planes of the hexagonal phase WS$_2$, respectively. The XRD pattern of the
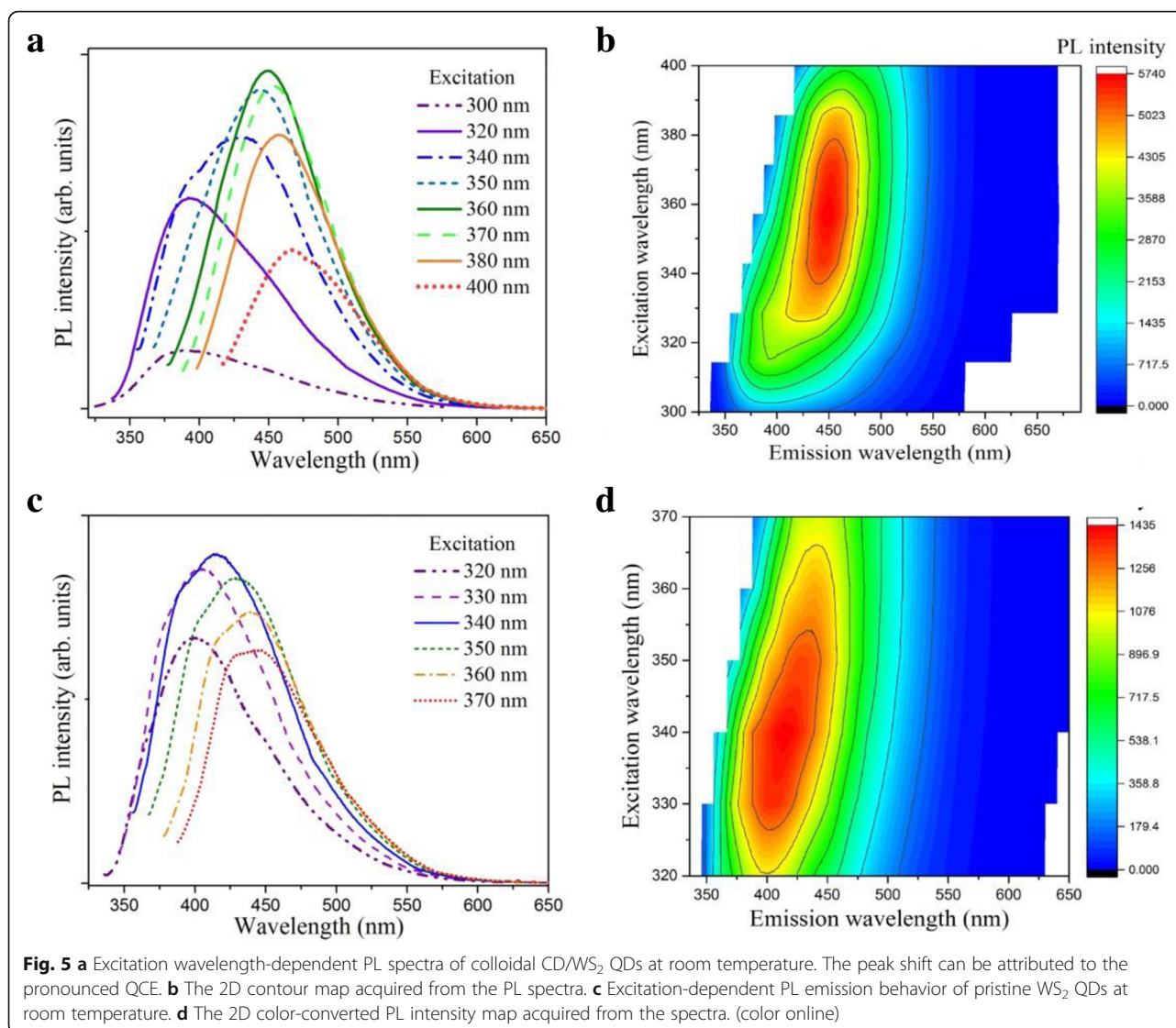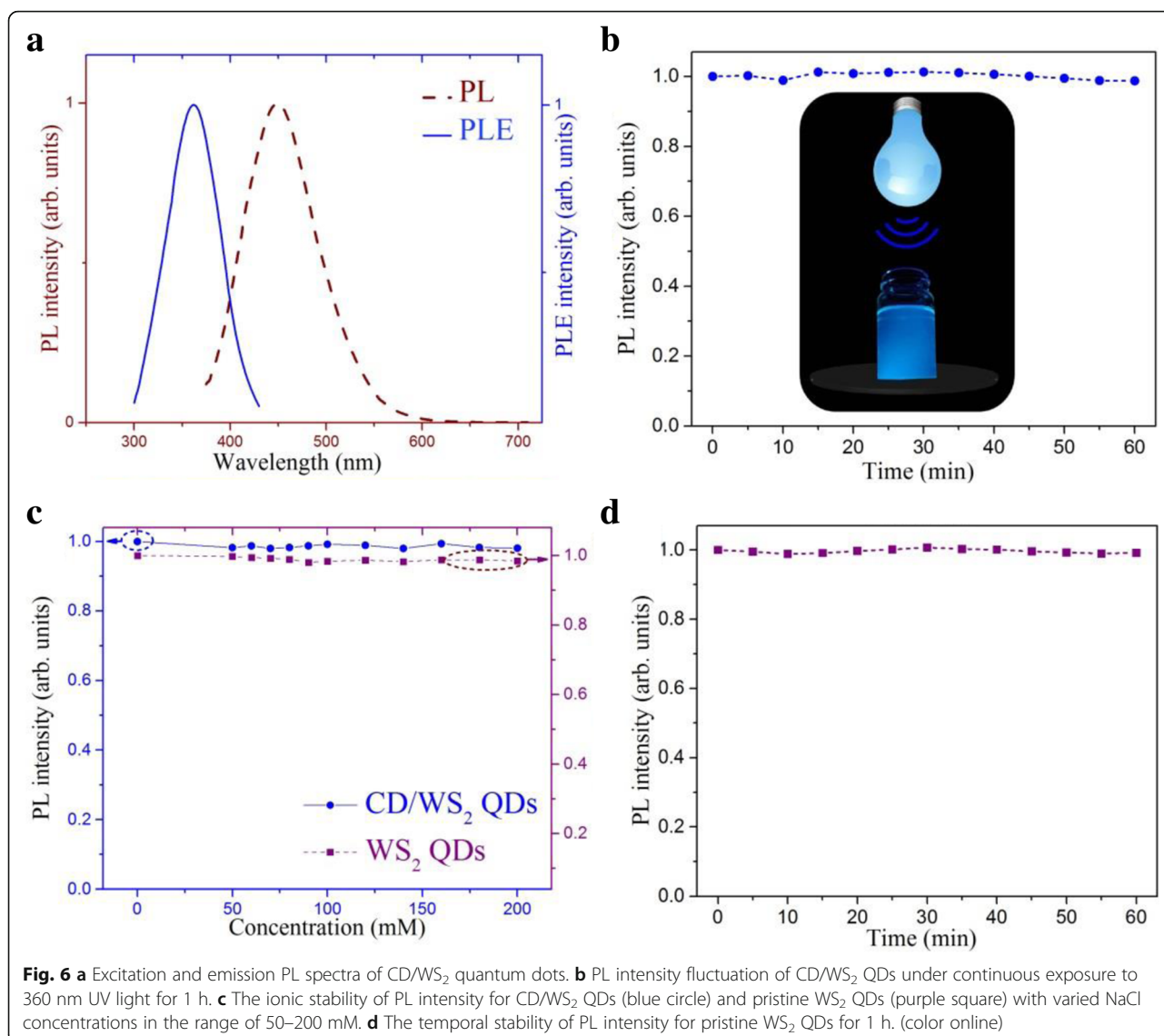
Fig. 5 a Excitation wavelength-dependent PL spectra of colloidal CD/WS$_2$ QDs at room temperature. The peak shift can be attributed to the pronounced QCE. **b** The 2D contour map acquired from the PL spectra. **c** Excitation-dependent PL emission behavior of pristine WS$_2$ QDs at room temperature. **d** The 2D color-converted PL intensity map acquired from the spectra. (color online)

nanocomposite shows that the intrinsic structure of 2H WS$_2$ was well retained during the synthesis reaction. For these prepared QD samples, the (002) diffraction peak was not resolved. A few studies have reported similar disappearance or strong suppression of the characteristic (002) diffraction peak for monolayer TMD nanosheets and quantum dots [51–53]. Furthermore, the reflections marked by asterisks were ascribed to the L-cysteine compound [54, 55]. Finally, the thickness of the as-synthesized WS$_2$ QDs was checked by atomic force microscopy (AFM) analysis. The AFM height profile shown in Fig. 2b reveals the particle thickness ranging from 6 to 10 nm, which indicates the presence of few-layered QD structure and is close to the TEM results.

Surface Elemental and Valence State Analysis

In order to determine the chemical composition and valence states of the elements in the pristine WS$_2$ and the CD/WS$_2$ QDs, X-ray photoelectron spectroscopy (XPS) analysis was carried out. Figure 3a shows the whole XPS survey spectra of WS$_2$ QDs and the CD/WS$_2$ QDs. Here, the presence of W, S, C, and O was detected for our synthesized QDs. In the high-resolution W 4f core level spectrum of CD/WS$_2$ QDs, the main peak can be deconvoluted to two contributed bands at 33.5 eV and 34.1 eV, as shown in Fig. 3b. They can be assigned to W 4f$_{7/2}$ and W 4f$_{5/2}$ states, and thus confirms the presence of W^{4+} in CD/WS$_2$ QDs [41, 56]. One more peak located at 35.7 eV can be assigned to W 5p$_{3/2}$. This can be attributed to the W^{6+} species in the samples [32, 57]. As for the high-resolution S 2p core level spectrum in Fig. 3c, four characteristic peaks with binding energies at 161.9, 163.1, 165.7, and 166.9 eV can be resolved. The S 2p peaks at 161.9 eV and 163.1 eV correspond to S 2p$_{3/2}$ and S 2p$_{1/2}$ orbitals of divalent sulfide ions [37, 58]. Together with the binding energy split of 1.2 eV, it indicates the S^{2-} oxidation

Hang *et al. Nanoscale Research Letters* (2019) 14:271

Page 8 of 15

Fig. 6 a Excitation and emission PL spectra of CD/WS$_2$ quantum dots. **b** PL intensity fluctuation of CD/WS$_2$ QDs under continuous exposure to 360 nm UV light for 1 h. **c** The ionic stability of PL intensity for CD/WS$_2$ QDs (blue circle) and pristine WS$_2$ QDs (purple square) with varied NaCl concentrations in the range of 50–200 mM. **d** The temporal stability of PL intensity for pristine WS$_2$ QDs for 1 h. (color online)

state in QDs [11, 37]. Meanwhile, the binding energy at 165.7 eV suggests the existence of bridging disulfides S$_2^{2-}$ and/or apical S^{2-} ligands, which may be related to active edge sites [43, 59]. As for the high-energy component at 166.9 eV, it can be ascribed to S^{4+} species in sulfate groups (SO$_3^{2-}$), which could locate at edges of WS$_2$ QDs [59]. High-resolution spectrum of C 1s is displayed in Fig. 3d. A multiple-peak analysis showed three peaks. The main binding energy peak at 284.7 eV is ascribed to C-C bond, which is due to the carbon atom in graphitic structures. The secondary peak at 286.2 eV is assigned to C-O and/or C-N. Additionally, a minute contribution located at 288.0 eV suggests the presence of C=O bond. The existence of these C 1s peaks is very close to what has been reported for C-dots in the literature [46]. In the case of pristine WS$_2$ QDs, analogous XPS spectra shapes were obtained. Figure 3e illustrates the high-resolution W 4f spectrum. It

consists of three bands centered at 33.5, 34.2, and 35.8 eV that correspond to the W 4f$_{7/2}$, W 4f$_{5/2}$, and W 5p$_{3/2}$ orbitals, which is reminiscent of hybrid CD/WS$_2$ QDs. From Fig. 3f, the fitted peak positions of the detected S 2p spectrum also nearly coincide with the binding energies for pristine WS$_2$ QDs. The similarity here hints that the hybridization was mainly realized by a physical adsorption of CDs onto the WS$_2$ QD surface instead of formation of covalent bond between the constituting components [30]. The overall XPS results agree with those reported for 2H-WS$_2$ and indicate the successful synthesis of WS$_2$ QDs [32, 41].

Optical Property Studies

Optical features of WS$_2$ QDs were studied by optical absorption and photoluminescence (PL) measurements. The UV–Vis spectra of our WS$_2$ QDs were depicted in
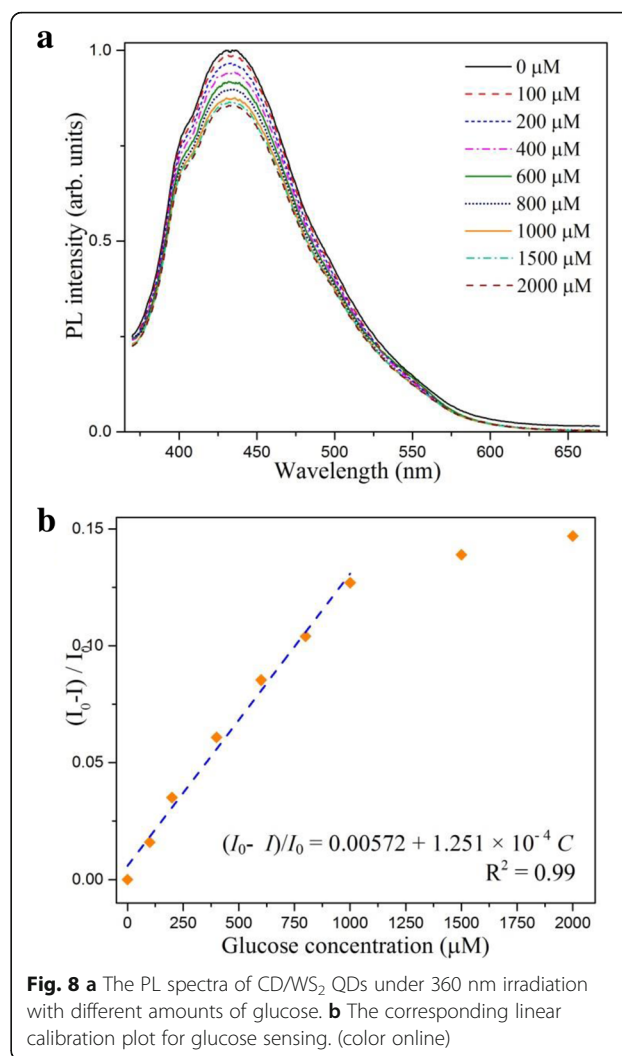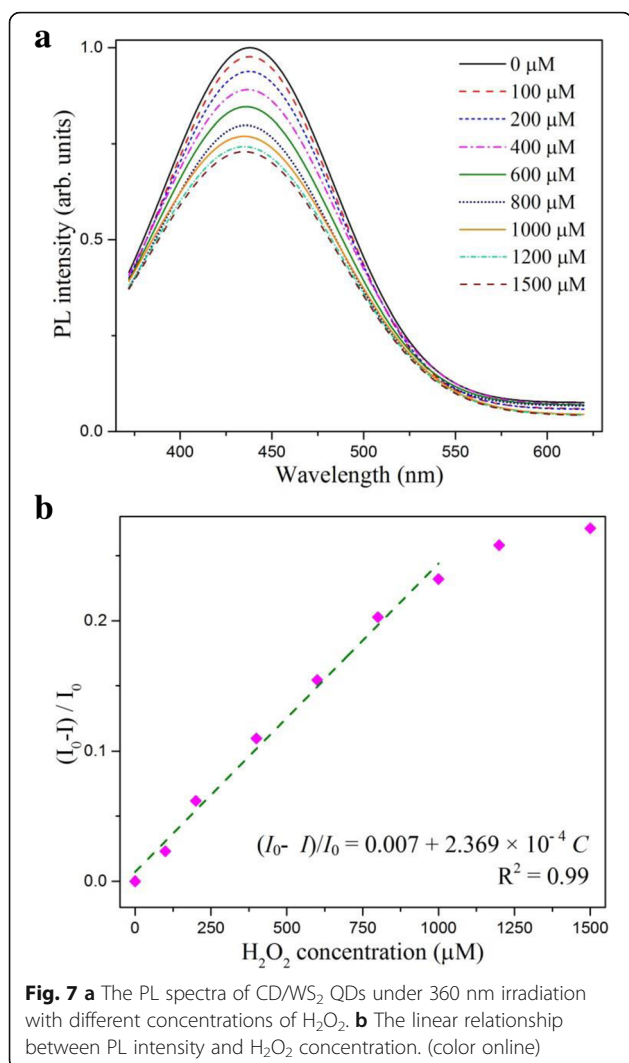
Hang *et al. Nanoscale Research Letters* (2019) 14:271

Page 9 of 15

Fig. 7 a The PL spectra of CD/WS$_2$ QDs under 360 nm irradiation with different concentrations of H$_2$O$_2$. **b** The linear relationship between PL intensity and H$_2$O$_2$ concentration. (color online)

Fig. 8 a The PL spectra of CD/WS$_2$ QDs under 360 nm irradiation with different amounts of glucose. **b** The corresponding linear calibration plot for glucose sensing. (color online)

Fig. 4. In general, appearance of four characteristic excitonic absorption bands in visible range is expected for WS$_2$ microcrystals and 2D nanosheets. Here, the excitonic peaks disappear and dominant absorption bands in the near-UV region ($\lambda \approx 300$ nm) can be observed for as-prepared QDs. The strong absorption is assigned to transitions from the low-lying valence band to the conduction band in WS$_2$ QDs. The band-edge position is close to 360 nm, which is due to the quantum size effect. It is known that the optical absorption of TMD QDs exhibits a strong blue-shift when the lateral dimensions of the nanoparticles are less than around 20 nm [50]. As the majority of our fabricated QD sizes are within the quantum confinement regime, a large blue-shift is expected and confirmed.

PL spectroscopy provides a contactless optical means to investigate the electronic structure of semiconductor materials. The PL spectra of the synthesized CD/WS$_2$ QD dispersions were taken at room temperature under different excitation wavelengths, as shown in Fig. 5a. As the excitation wavelength was switched from 300 to 400 nm, the emission peak is gradually redshifted from 385 to 470 nm. Analogous excitation-dependent fluorescence emissions have been found in a few TMD QD reports [22, 60]. As found in our UV–Vis results, the QCE strongly affects the band gap of our QDs. A longer wavelength resonantly excites larger QDs with narrower band gaps, leading to emissions peaked at longer wavelengths. Accordingly, the emission peak progressively redshift as the excitation wavelength is increased as a result of the QCE. This trend of PL intensity in response to varied excitation energy is clearly revealed by the 2D color-converted PL contour map as depicted in Fig. 5b. The strongest emission appears at 450 nm (2.58 eV) with an excitation wavelength of 360 nm. The emission may be attributed to excitonic transitions between the minimum of conduction band to the uppermost split valence bands (A and B excitons) [22]. To have deeper insight
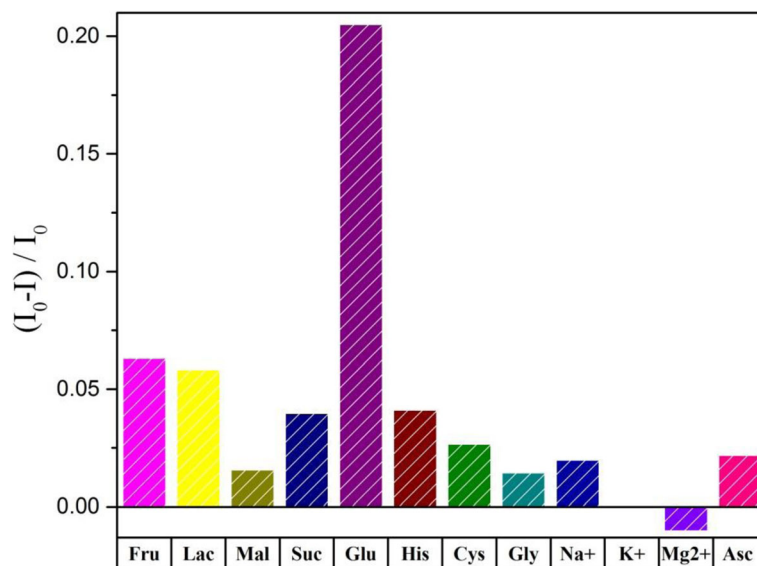
Fig. 9 Selectivity tests for glucose detection using other sugars and some usual species as control. (color online)

into the nature of the electronic transitions, PL excitation (PLE) was carried out by using the detection wavelength set at characteristic emission position. Figure 6a displays the PLE spectrum under the detection wavelength of 450 nm. We found an evident PLE peak around 360 nm, which agrees well with the UV–Vis result. It further hints that the strong emission originated from excitonic A emission of QDs [22].

Under irradiation of UV light, a strong blue luminescence can be easily observed by the naked eye, as depicted in the inset of Fig. 6b. It is known that WS_2 in its bulk form has very limited luminescent intensity. The strong blue emission again supports the successful fabrication of nanostructures in quantum confinement regime. The stability of luminescence is essential in the optical sensing application. The photo stability of CD/WS_2 QDs was checked by the time-dependent PL measurement under an excitation of 360 nm. Figure 6b shows that the luminescent intensity is almost unchanged after UV irradiation for 1 h. Next, we study the effect of salt solution on the fluorescence intensity of QDs. As presented in Fig. 6c, the CD/WS_2 QDs possess good ionic stability under different concentrations of NaCl solution, revealing the potential for sensing in a physiological environment. These results suggest that the PL properties of our synthetic QDs can be employed for luminescence sensing purpose. Parallel PL properties were found for pristine WS_2 QDs except the luminescent intensity is weaker than that of hybrid QDs. Excitation wavelength-dependent PL spectra of pristine WS_2 QDs are shown in Fig. 5c. Figure 5d displays the 2D PL contour map derived from the PL spectra of WS_2 QDs, which shows a

prominent red-shift with an increase in the excitation wavelength. Good ionic and temporal stability in luminescent intensity was also found for pristine WS_2 QDs, which is shown in Fig. 6c, d, respectively. The PL quantum yields of WS_2 QDs and CD/WS_2 QDs are 3.05% and 4.1% using quinine sulfate as a reference at the excitation wavelength of 360 nm (theoretical quantum yield 54%).

Application to H_2O_2 and Glucose Detection

Different concentrations of H_2O_2 were added into both types of WS_2 QD solutions to evaluate the capability of prepared QDs for luminescence sensing. Figure 7a shows that the PL intensity of the CD/WS_2 QDs monotonically decreased with increasing the concentration of H_2O_2 from 0.1 to 1 mM. The relationship between the H_2O_2 concentration and PL intensity is depicted in Fig. 7b. We found the dependence can be fitted as a linear function as $(I_0 - I)/I_0 = 0.007 + 2.369 \times 10^{-4} C$ with a correlation coefficient of $R^2 = 0.99$, where I_0 and I were the PL intensity of sensing system in the absence and presence of target molecules, respectively. The detection limit is estimated to be 40 μM. For pristine WS_2 QDs, the PL spectra with varied concentrations of H_2O_2 are shown in Additional file 1: Figure S1 (a). A good linear relationship was also obtained in the same concentration range with $R^2 = 0.99$ and a detection limit of 60 μM was assessed, as presented in Additional file 1: Figure S1 (b). The linear detection range is quite similar to a recent H_2O_2 optical sensing study on the use MoS_2 QDs [24].

The developed fluorescence sensing system was further extended to the measurement of glucose. In the

Hang *et al. Nanoscale Research Letters* (2019) 14:271

Page 11 of 15

a

b

Fig. 10 a Time-resolved PL spectra of CD/WS$_2$ QDs with and without the presence of hydrogen peroxide. **b** PL decay curve in the absence of hydrogen peroxide (orange dots). The dashed line represents the fit to the experimental data. (color online)
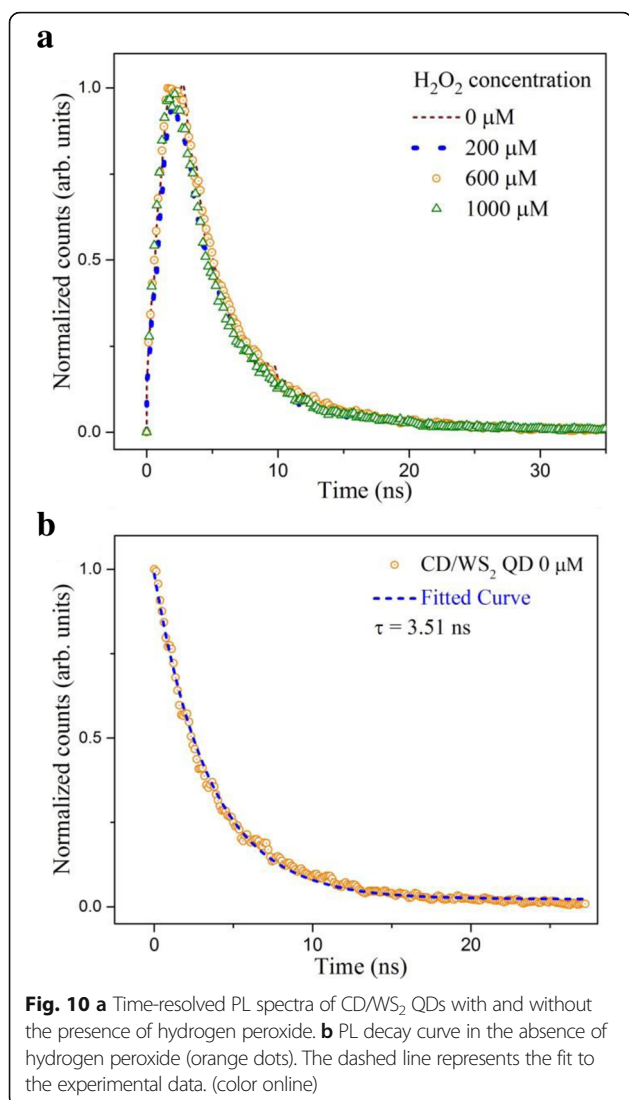
presence of glucose oxidase (GOx) in solution, glucose can be oxidized to gluconic acid with dissolved oxygen, as illustrated in Scheme 1. The main reaction product H$_2$O$_2$ can then trigger the PL quenching of WS$_2$ QDs in proportion, which serves as the basis for glucose detection. The PL intensity of the CD/WS$_2$ QDs with different amount of glucose is shown in Fig. 8a. In the company of GOx, the PL intensity decreased progressively with the increase of the concentration of glucose from 0.1 to 1 mM, which is due to the increasing amount of produced H$_2$O$_2$. Figure 8b exhibits a good linear relationship between the quenching efficiency and glucose concentration (R^2 = 0.99 and LOD = 60 μM). As for pristine WS$_2$ QDs, the glucose concentration-dependent PL spectra are displayed in Additional file 1: Figure S2 (a). There exists a good linear relationship in the concentration range of 0.8 to 8 mM, as shown in Additional file 1: Figure S2 (b). This LOD is larger than

that of CD/WS$_2$ QDs. Our result shows that CD/WS$_2$ QDs provide a more sensitive LOD for glucose detection while pristine WS$_2$ QDs works better for larger dynamic range.

To further assess the selectivity of this glucose sensing platform, control experiments were carried out to compare the quenching efficiency induced by fructose, lactose, maltose, and some other species. As illustrated in Fig. 9, these glucose analogs caused little impact on glucose detection, which is due to the high affinity of GOx. Meanwhile, the others posed insignificant changes in the probe signals. Therefore, our results suggest that WS$_2$ QDs can be employed as an alternative platform for the optical determination of glucose level.

Time-Resolved PL and Raman Studies

To further explore the photo physical properties of the fluorescence system, more optical investigations were imposed. Time-resolved PL (TRPL) was recorded at the strongest emission wavelength ≈ 450 nm by using an excitation wavelength of 360 nm. The TRPL spectrum of CD/WS$_2$ QD solutions was depicted as the brown dashed line in Fig. 10a. The decay behavior indicates a nanosecond-scale lifetime of luminescence. Its decay kinetics can be fitted well with a single exponential decay function, as plotted in Fig. 10b. The lifetime of luminescence was estimated to be 3.51 ns. Moreover, we found that when the QD solutions were treated with different concentrations of H$_2$O$_2$, no eloquent changes could be observed to the PL decay curves. Calculated lifetimes of TRPL spectra were summarized in Additional file 1: Table S1. Identical properties were also observed for pristine WS$_2$ QDs, as shown in Additional file 1: Figure S3. Our results indicate that the recombination dynamics in QDs are barely affected by hydrogen peroxide so that the lifetime of photo-generated excitons is almost unchanged. As a consequence, the suppression of PL cannot be ascribed to a reduction in transition rate or an increase in nonradiative traps [61].

Raman spectroscopy has been frequently employed to extract additional complementary information of ultrathin 2D-layered nanomaterials [62]. In general, for 2D-layered TMD compounds, there are four Raman-active modes, specifically A$_{1g}$, E$_{1g}$, E$^1_{2g}$, and E$^2_{2g}$ modes [62, 63]. E$_{1g}$ mode is hardly found in 2D nanosheet reports because of forbidden selection rule in the typical back-scattering measurement geometry. The representative Raman spectra of pristine WS$_2$ and CD/WS$_2$ QDs were displayed in Fig. 11. Two major peaks at 353 cm^{-1} and 420 cm^{-1} reveal the clear signature of WS$_2$ in all the prepared samples. The inset sketch illustrates the two principal Raman-active modes of WS$_2$, which lead to the two peaks in the Raman spectra. The A$_{1g}$ mode at 420 cm^{-1} results from the out-of-plane vibration of S atoms in opposite direction. Besides, we
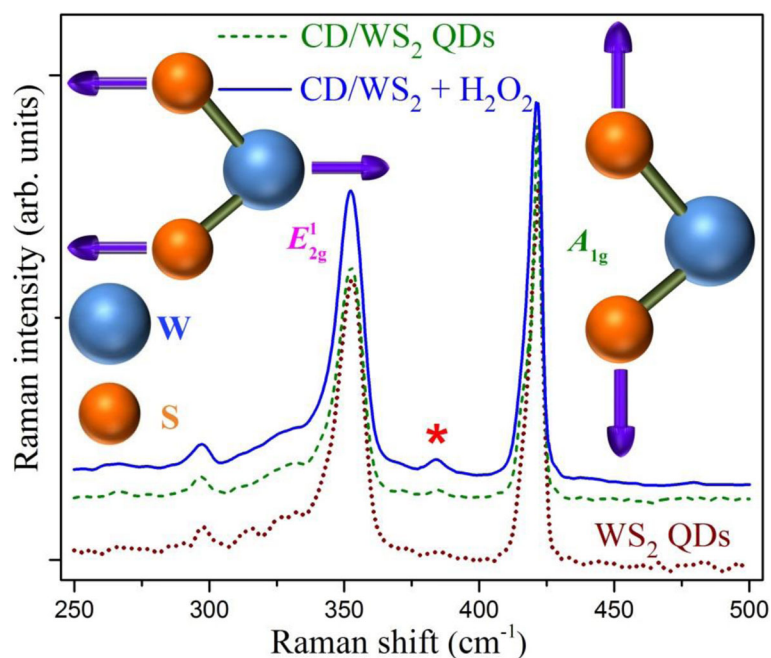
Fig. 11 Raman spectra of WS$_2$ QDs and CD/WS$_2$ QDs. The Raman spectrum of CD/WS$_2$ QDs after hydrogen peroxide treatment is shown as the solid line. The inset sketch illustrates the atomic displacements for the two vibrational modes responsible for the primary Raman peaks. (color online)

observed small shoulder on the lower-frequency side of the A$_{1g}$ peak, which arises due to Davydov splitting as reported earlier [64, 65]. Due to the lattice stiffening effect of the A$_{1g}$ mode, the Raman shift between the main A$_{1g}$ and the in-plane E$^1_{2g}$ modes has been employed as an indicator of WS$_2$ thickness [66, 67]. Here, the energy splitting between the two peaks are almost identical and the frequency difference of 67 cm^{-1} suggests the few-layer structure of our WS$_2$-based QDs [67]. Another proposed gauge of sample thickness is the ratio of the intensity of A$_{1g}$ mode to that of E$^1_{2g}$ mode. The A$_{1g}$ peak is 1.35 and 1.6 times the height of the E$^1_{2g}$ peak for WS$_2$ and CD/WS$_2$ QDs, respectively. It also reveals the few-layer nature of our synthesized QD structures [67]. Notably, the slightly larger Raman peak ratio of CD/WS$_2$ QDs reflects the increased physical thickness of WS$_2$ QDs in the hybridization process. The common weak feature at 297 cm^{-1} is close to the E$_{1g}$ mode whose appearance could be related to 2D few-layer QD structure [68, 69]. Similar feature found by other group has been proposed to be a multi-phonon scattering mode [70]. Here, both modes may coexist in our Raman observation [69].

One other interesting characteristic was noted in the Raman scattering results of CD/WS$_2$ QDs after H$_2$O$_2$ treatment. As designated by an asterisk in Fig. 11, there exists an identifiable signal at 385 cm^{-1}, which is attributable to neither first-order nor second-order WS$_2$ Raman scattering modes [68]. This peak can be ascribed to the bending (δ) mode O–W–O in WS$_2$ QDs [71, 72],

whose presence indicates the formation of W–O bonds upon H$_2$O$_2$ treatment. This mode became obviously pronounced because of the oxidation induced by hydrogen peroxide. As edge states are abundant in ultrathin 2D QDs, partial oxidation or doping of oxygen is facilitated in the reactions with hydrogen peroxide. It is in sharp contrast with 2D nanosheets because sheet surfaces are not very sensitive to oxidation. Recently, a first-principles calculation showed that the band structure of partially oxidized MoS$_2$ QDs can be modified, leading to the suppression of photoluminescence by hydrogen peroxide treatment [61]. It was shown that with certain degree of oxidation, the high efficient direct bandgap structure of MoS$_2$ QDs can become inefficient indirect bandgap structure with certain bandgap narrowing. In this case, the photoluminescence of oxidized MoS$_2$ QDs can be quenched and additional longer wavelength absorption could be found. These effects predicted by the above-mentioned calculations are consistent with our experimental outcome in partially oxidized WS$_2$ QDs. Analogous mechanism is very likely to occur in our case since general features of the WS$_2$ band structure are similar to those of MoS$_2$. Furthermore, we found the corresponding absorption band of two types of WS$_2$ QDs appeared red-shift after H$_2$O$_2$ was added to the solution, as shown by the dashed lines in Fig. 4. As a comparison, the absorption data of sole hydrogen peroxide was included as the brown dashed dot line, which indicates that the change is not due to the presence of

Hang *et al. Nanoscale Research Letters* (2019) 14:271

Page 13 of 15

H_2O_2 alone. Same behavior was recently reported for oxidation-induced luminescence quenching of MoS_2 QDs [24]. Consequently, oxidation induced by hydrogen peroxide is accounted for the sensing mechanism of our WS_2 QDs by using PL quenching.

Conclusions

In summary, for the first time, photoluminescent WS_2 QDs and CD/WS_2 QDs were prepared under "bottom-up" hydrothermal conditions by using sodium tungstate dihydrate and L-cysteine. From the TEM analysis, it can be observed that the synthesized WS_2 QDs had high crystallinity and featured good dispersibility. On the basis of the strong PL with high stability from as-prepared QDs, they were subsequently applied for the construction of an electrodeless PL quenching sensor for detection of H_2O_2 and glucose. Both types of QDs show similar capability in H_2O_2 sensing and hybrid CD/WS_2 QDs provide a more sensitive LOD for glucose detection. The stability test showed that the produced WS_2-based QDs are robust against photo-degradation and is stable during the sensing period. The Raman study implied that H_2O_2 causes the partial oxidation of QDs, which may lead to oxidation-induced quenching. Compared with most reported works with "top-down" approaches, the proposed "bottom-up" protocol for WS_2-based QDs has the advantages of simple preparation, low cost, eco-friendliness, and ease for hybrid construction. Furthermore, these water-soluble WS_2-based QDs with abundant active sites can be a promising candidate for potential applications in environmental monitoring, biochemistry, and clinical diagnostics. For instance, as there exist numerous kinds of O_2-dependent oxidases which generates hydrogen peroxide, the presented facile 0D QDs may also be employed to detect other target molecules by taking the corresponding enzymes. Overall, our results provide an alternative and cost-efficient platform to exploit the diverse functionalities of 0D WS_2-based nanomaterials. Further structural layout and extended applications are underway.

Additional file

Additional file 1: Figure S1. (a) PL spectra of WS2 QDs under 360 nm irradiation with different concentrations of H2O2. (b) The linear calibration plot for H2O2 concentration. **Figure S2.** (a) The PL spectra of WS_2 QDs under 360 nm irradiation with different amounts of glucose. (b) The correlation between PL quenching ratios and the concentration of glucose. **Figure S3.** Time-resolved PL spectra of WS_2 QDs treated with an increasing concentration of hydrogen peroxide. **Table S1.** Calculated lifetime of TRPL spectra of CD/WS_2 QDs treated with varied concentration of hydrogen peroxide. (DOCX 404 kb)

Abbreviations

AFM: Atomic force microscopy; CD: Carbon quantum dot; GOx: Glucose oxidase; HRTEM: High-resolution transmission electron microscopy; PL: Photoluminescence; PLE: Photoluminescence excitation; QCE: Quantum confinement effect; QDs: Quantum dots; TEM: Transmission electron microscopy; TMD: Transition metal dichalcogenide; TRPL: Time-resolved photoluminescence; UV–Vis: Ultraviolet-visible; XPS: X-ray photoelectron spectroscopy; XRD: X-ray diffractometer

Authors' Contributions
DRH directed the project and finalized this manuscript. DYS and DRH conceived and designed the experiments. DYS carried out the main part of the experiments. CHC and HFW provided equipment support in the synthesis work. MMCC helped to polish the manuscript. SEI and KHS gave suggestions on the experimental design. All authors read and approved the final manuscript.

Availability of Data and Materials
All data generated or analyzed during this study are included in this published article and its supplementary information file.

Competing Interests
The authors declare that they have no conflict of interests.

Author details
[1]Department of Materials and Optoelectronic Science, National Sun Yat-sen University, Kaohsiung 80424, Taiwan. [2]Center of Crystal Research, National Sun Yat-sen University, Kaohsiung 80424, Taiwan. [3]Department of Chemistry, National Sun Yat-sen University, Kaohsiung 80424, Taiwan.

References
1. Novoselov KS, Geim AK, Morozov SV, Jiang D, Zhang Y, Dubonos SV, Grigorieva IV, Firsov AA (2004) Electric field effect in atomically thin carbon films. Science 306:666–669
2. Chuang C, Yang Y, Pookpanratana S, Hacker CA, Liang C-T, Elmquist RE (2017) Chemical-doping-driven crossover from graphene to "ordinary metal" in epitaxial graphene grown on SiC. Nanoscale 9:11537–11544
3. Liu C-W, Chuang C, Yang Y, Elmquist RE, Ho YJ, Lee H-Y, Liang C-T (2017) Temperature dependence of electron density and electron-electron interactions in monolayer epitaxial graphene grown on SiC. 2D Mater 4:025007
4. Han JH, Kwak M, Kim Y, Cheon J (2018) Recent advances in the solution-based preparation of two-dimensional layered transition metal chalcogenide nanostructures. Chem Rev 118:6151–6188
5. Hang D-R, Sharma KH, Chen C-H, Islam SE (2016) Enhanced photocatalytic performance of ZnO nanorods coupled by two-dimensional α-MoO₃ nanoflakes under UV and visible light irradiation. Chem Eur J 22:12777–12784
6. Mei J, Liao T, Kou L, Sun Z (2017) Two-dimensional metal oxide nanomaterials for next generation rechargeable batteries. Adv Mater 29:1700176
7. Kalantar-zadeh K, Ou JZ, Daeneke T, Mitchell A, Sasaki T, Fuhrer MS (2016) Two dimensional and layered transition metal oxides. Appl Mater Today 5:73–89
8. Ong W-J, Tan L-L, Ng YH, Yong S-T, Chai S-P (2016) Graphitic carbon nitride (g-C₃N₄)-based photocatalysts for artificial photosynthesis and environmental remediation: are we a step closer to achieving sustainability? Chem Rev 116:7159–7329
9. Radisavljevic B, Radenovic A, Brivio J, Giacometti V, Kis A (2011) Single-layer MoS₂ transistors. Nat Nanotechnol 6:147–150
10. Kalantar-zadeh K, Ou JZ (2016) Biosensors based on two-dimensional MoS₂. ACS Sens 1:5–16
11. Islam SE, Hang D-R, Chen C-H, Sharma KH (2018) Facile and cost-efficient synthesis of quasi-0D/2D ZnO/MoS₂ nanocomposites for highly enhanced visible-light-driven photocatalytic degradation of organic pollutants and antibiotics. Chem Eur J 24:9305–9315
12. Teo WZ, Chng EL, Sofer Z, Pumera M (2014) Cytotoxicity of exfoliated transition-metal dichalcogenides (MoS₂, WS₂, and WSe₂) is lower than that of graphene and its analogues. Chem Eur J 20:9627–9632

13. Zhu L, Zhang Y, Xu P, Wen W, Li X, Xu J (2016) PtW/MoS$_2$ hybrid nanocomposite for electrochemical sensing of H$_2$O$_2$ released from living cells. Biosens Bioelectron 80:601–606

14. Gan X, Zhao H, Quan X (2017) Two-dimensional MoS$_2$: a promising building block for biosensors. Biosens Bioelectron 89:56–71

15. Peng J, Weng J (2017) Enhanced peroxidase-like activity of MoS$_2$/graphene oxide hybrid with light irradiation for glucose detection. Biosens. Bioelectron 89:652–658

16. Mao L, Osborne PG, Yamamoto K, Kato T (2002) Continuous on-line measurement of cerebral hydrogen peroxide using enzyme-modified ring–disk plastic carbon film electrode. Anal Chem 74:3684–3689

17. Sharma AK, Pandey S, Sharma KH, Nerthigan Y, Khan MS, Hang D-R, Wu H-F (2018) Two dimensional α-MoO$_{3-x}$ nanoflakes as bare eye probe for hydrogen peroxide in biological fluids. Anal Chim Acta 1015:58–65

18. Nerthigan Y, Sharma AK, Pandey S, Sharma KH, Khan MS, Hang D-R, Wu H-F (2018) Glucose oxidase assisted visual detection of glucose using oxygen deficient α-MoO$_{3-x}$ nanoflakes. Microchim Acta 185:65

19. Li BL, Setyawati MI, Zou HL, Dong JX, Luo HQ, Li NB, Leong DT (2017) Emerging 0D transition-metal dichalcogenides for sensors, biomedicine, and clean energy. Small 13:1700527

20. Xu Y, Wang X, Zhang WL, Lv F, Guo S (2018) Recent progress in two-dimensional inorganic quantum dots. Chem Soc Rev 47:586–625

21. Gan ZX, Liu LZ, Wu HY, Hao YL, Shan Y, Wu XL, Chu PK (2015) Quantum confinement effects across two-dimensional planes in MoS$_2$ quantum dots. Appl Phys Lett 106:233113

22. Huang H, Du C, Shi H, Feng X, Li J, Tan Y, Song W (2015) Water-soluble monolayer molybdenum disulfide quantum dots with upconversion fluorescence. Part Part Syst Charact 32:72–79

23. Wang Y, Ni Y (2014) Molybdenum disulfide quantum dots as a photoluminescence sensing platform for 2,4,6-trinitrophenol detection. Anal Chem 86:7463–7470

24. Wang X, Wu Q, Jiang K, Wang C, Zhang C (2017) One-step synthesis of water-soluble and highly fluorescent MoS$_2$ quantum dots for detection of hydrogen peroxide and glucose. Sens Actuators B 252:183–190

25. Eftekhari A (2017) Tungsten dichalcogenides (WS$_2$, WSe$_2$, and WTe$_2$): materials chemistry and applications. J Mater Chem A 5:18299–18325

26. Khalil HMW, Khan MF, Eom J, Noh H (2015) Highly stable and tunable chemical doping of multilayer WS$_2$ field effect transistor: reduction in contact resistance. ACS Appl Mater Interfaces 7:23589–23596

27. Yao J, Zheng Z, Yang G (2016) Layered-material WS$_2$/topological insulator Bi$_2$Te$_3$ heterostructure photodetector with ultrahigh responsivity in the range from 370 to 1550 nm. J Mater Chem C 4:7831–7840

28. Lan C, Li C, Wang S, He T, Zhou Z, Wei D, Guo H, Yang H, Liu Y (2017) Highly responsive and broadband photodetectors based on WS$_2$–graphene van der Waals epitaxial heterostructures. J Mater Chem C 5:1494–1500

29. Sang Y, Zhao Z, Zhao M, Hao P, Leng Y, Liu H (2015) From UV to near-infrared, WS$_2$ nanosheet: a novel photocatalyst for full solar light spectrum photodegradation. Adv Mater 27:363–369

30. Atkin P, Daeneke T, Wang Y, Carey BJ, Berean KJ, Clark RM, Ou JZ, Trinchi A, Cole IS, Kalantar-zadeh K (2016) 2D WS$_2$/carbon dot hybrids with enhanced photocatalytic activity. J Mater Chem A 4:13563–13571

31. Ma J, Yu H, Jiang X, Luo Z, Zheng Y (2019) High sensitivity label-free detection of Fe3+ ion in aqueous solution using fluorescent MoS$_2$ quantum dots. Sens. Actuators B 281:989–997

32. Lin L, Xu Y, Zhang S, Ross IM, Ong ACM, Allwood DA (2013) Fabrication of luminescent monolayered tungsten dichalcogenides quantum dots with giant spin-valley coupling. ACS Nano 7:8214–8223

33. Ghorai A, Bayan S, Gogurla N, Midya A, Ray SK (2017) Highly luminescent WS$_2$ quantum dots/ZnO heterojunctions for light emitting devices. ACS Appl Mater Interfaces 9:558–565

34. Zhang X, Lai Z, Tan C, Zhang H (2016) Solution-processed two-dimensional MoS$_2$ nanosheets: preparation, hybridization, and applications. Angew Chem Int Ed 55:8816–8838

35. Wang M, Xu X, Ge Y, Dong P, Baines R, Ajayan PM, Ye M, Shen J (2017) Surface tension components ratio: an efficient parameter for direct liquid phase exfoliation. ACS Appl Mater Interfaces 9:9168–9175

36. O'Neill A, Khan U, Coleman JN (2012) Preparation of high concentration dispersions of exfoliated MoS$_2$ with increased flake size. Chem Mater 24:2414–2421

37. Xu S, Li D, Wu P (2015) One-pot, facile, and versatile synthesis of monolayer MoS$_2$/WS$_2$ quantum dots as bioimaging probes and

38. efficient electrocatalysts for hydrogen evolution reaction. Adv Funct Mater 25:1127–1136

38. Zhang X, Lai Z, Liu Z, Tan C, Huang Y, Li B, Zhao M, Xie L, Huang W, Zhan H (2015) A facile and universal top-down method for preparation of monodisperse transition-metal dichalcogenide nanodots. Angew Chem Int Ed 54:5425–5428

39. Stengl V, Tolasz J, Popelkova D (2015) Ultrasonic preparation of tungsten disulfide single-layers and quantum dots. RSC Adv 5:89612–89620

40. Yan Y, Zhang C, Gu W, Ding C, Li X, Xian Y (2016) Facile synthesis of water-soluble WS$_2$ quantum dots for turn-on fluorescent measurement of lipoic acid. J Phys Chem C 120:12170–12177

41. Guo X, Wang Y, Wu F, Ni Y, Kokot S (2015) The use of tungsten disulfide dots as highly selective, fluorescent probes for analysis of nitrofurazone. Talanta 144:1036–1043

42. Duan X, Liu Q, Wang G, Su X (2019) WS$_2$ quantum dots as a sensitive fluorescence probe for the detection of glucose. J Lumin 207:491–496

43. Zhao S, Li C, Wang L, Liu N, Qiao S, Liu B, Huang H, Liu Y, Kang Z (2016) Carbon quantum dots modified MoS$_2$ with visible-light-induced high hydrogen evolution catalytic ability. Carbon 99:599–606

44. Sahatiya P, Jones SS, Badhulika S (2018) 2D MoS$_2$–carbon quantum dot hybrid based large area, flexible UV–vis–NIR photodetector on paper substrate. Appl Mater Today 10:106–114

45. Canton-Vitoria R, Vallan L, Urriolabeitia E, Benito AM, Maser WK, Tagmatarchis N (2018) Electronic interactions in illuminated carbon dot/MoS$_2$ ensembles and electrocatalytic activity towards hydrogen evolution. Chem Eur J 24:10468–10474

46. Roy P, Chen PC, Periasamy AP, Chen YN, Chang HT (2015) Photoluminescent carbon nanodots: synthesis, physicochemical properties and analytical applications. Mater Today 18:447–458

47. Li H, Kang Z, Liu Y, Lee S-T (2012) Carbon nanodots: synthesis, properties and applications. J Mater Chem 22:24230

48. Bhaisare ML, Sharma KH, Lee J-Y, Hang D-R, Wu H-F (2016) Synthesis and characterization of two-dimensional carbon dots decorated with molybdenum oxide nanoflakes with various phases. New J Chem 40: 8954–8960

49. Hang D-R, Sharma KH, Islam SE, Chen C, Chou MMC (2014) Resonant Raman scattering and photoluminescent properties of nonpolar *a*-plane ZnO thin film on LiGaO$_2$ substrate. Appl Phys Express 7:041101

50. Valappil MO, Anil A, Shaijumon M, Pillai VK, Alwarappan S (2017) A single-step electrochemical synthesis of luminescent WS$_2$ quantum dots. Chem Eur J. 23:9144–9148

51. Lin H, Wang C, Wu J, Xu Z, Huang Y, Zhang C (2015) Colloidal synthesis of MoS$_2$ quantum dots: size-dependent tunable photoluminescence and bioimaging. New J Chem 39:8492–8497

52. Gopalakrishnan D, Damien D, Li B, Gullappalli H, Pillai VK, Ajayan PM, Shaijumon MM (2015) Electrochemical synthesis of luminescent MoS$_2$ quantum dots. Chem Commun 51:6293–6296

53. Dong H, Tang S, Hao Y, Yu H, Dai W, Zhao G, Cao Y, Lu H, Zhang X, Ju H (2016) Fluorescent MoS$_2$ quantum dots: ultrasonic preparation, up-conversion and down-conversion bioimaging, and photodynamic therapy. ACS Appl Mater Interfaces 8:3107–3114

54. Fan L, Deng M, Lin C, Xu C, Liu Y, Shi Z, Wang Y, Xu Z, Li L, He M (2018) A multifunctional composite Fe$_3$O$_4$/MOF/L-cysteine for removal, magnetic solid phase extraction and fluorescence sensing of Cd(II). RSC Adv 8:10561–10572

55. Arizaga GGC (2013) Synthesis of L-cystine nanotubes by alkalinization of L-cysteinein the presence of gallium nitride. J Cryst Growth 384:33–38

56. Ratha S, Rout CS (2013) Supercapacitor electrodes based on layered tungsten disulfide-reduced graphene oxide hybrids synthesized by a facile hydrothermal method. ACS Appl Mater Interfaces 5:11427–11433

57. Martinez H, Benayad A, Gonbeau D, Vinatier P, Pecquenard B, Levasseur A (2004) Influence of the cation nature of high sulfur content oxysulfide thin films MO$_y$S$_z$ (M=W, Ti) studied by XPS. Appl Surf Sci 236:377–386

58. Li BL, Chen LX, Zou HL, Lei JL, Luo HQ, Li NB (2014) Electrochemically induced Fenton reaction of few-layer MoS$_2$ nanosheets: preparation of luminescent quantum dots via a transition of nanoporous morphology. Nanoscale 6:9831–9838

59. Zheng XL, Xu JB, Yan KY, Wang H, Wang ZL, Yang SH (2014) Space-confined growth of MoS$_2$ nanosheets within graphite: the layered hybrid of MoS$_2$ and graphene as an active catalyst for hydrogen evolution reaction. Chem Mater 26:2344–2353

60. Shinde DB, Pillai VK (2012) Electrochemical preparation of luminescent graphene quantum dots from multiwalled carbon nanotubes. Chem Eur J 18:12522–12528
61. Gan Z, Gui Q, Shan Y, Pan P, Zhang N, Zhang L (2016) Photoluminescence of MoS_2 quantum dots quenched by hydrogen peroxide: A fluorescent sensor for hydrogen peroxide. J Appl Phys 120:104503
62. Frey GL, Tenne R, Matthews MJ, Dresselhaus MS, Dresselhaus G (1999) Raman and resonance Raman investigation of MoS_2 nanoparticles. Phys Rev B 60:2883–2892
63. Wang YC, Ou JZ, Balendhran S, Chrimes AF, Mortazavi M, Yao DD, Field MR, Latham K, Bansal V, Friend JR, Zhuiykov S, Medhekar NV, Strano MS, Kalantar-zadeh K (2013) Electrochemical control of photoluminescence in two-dimensional MoS(2) nanoflakes. ACS Nano 7:10083–10093
64. Staiger M, Gillen R, Scheuschner N, Ochedowski O, Kampmann F, Schleberger M, Thomsen C, Maultzsch J (2015) Splitting of monolayer out-of-plane A_1 Raman mode in few-layer WS_2. Phys Rev B 91:195419
65. Kim KW, Lee J-U, Nam DH, Cheong H (2016) Davydov splitting and excitonic resonance effects in Raman spectra of few-layer $MoSe_2$. ACS Nano 10:8113–8120
66. Lee C, Yan H, Brus LE, Heinz TF, Hone J, Ryu S (2010) Anomalous lattice vibrations of single- and few-layer MoS_2. ACS Nano 4:2695
67. Zeng HL, Liu GB, Dai JF, Yan YJ, Zhu BR, He RC, Xie L, Xu SJ, Chen XH, Yao W, Cui XD (2013) Optical signature of symmetry variations and spin-valley coupling in atomically thin tungsten dichalcogenides. Sci Rep 3:1608
68. Terrones H, Corro ED, Feng S, Poumirol JM, Rhodes D, Smirnov D, Pradhan NR, Lin Z, Nguyen MAT, Elías AL, Mallouk TE, Balicas L, Pimenta MA, Terrones M (2014) New first order Raman-active modes in few layered transition metal dichalcogenides. Sci Rep 4:4215
69. Yang J, Lee J-U, Cheong H (2017) Excitation energy dependence of Raman spectra of few-layer WS_2. FlatChem 3:64–70
70. Berkdemir A, Gutiérrez HR, Botello-Méndez AR, Perea-López N, Elías AL, Chia C-I, Wang B, Crespi VH, López-Urías F, Charlier J-C, Terrones H, Terrones M (2013) Identification of individual and few layers of WS_2 using Raman Spectroscopy. Sci Rep 3:1755
71. Berg RW, Maijó Ferré I, Schäffer SJC (2006) Raman spectroscopy evidence of 1:1:1 complex formation during dissolution of WO_3 in a melt of $K_2S_2O_7$: K_2SO_4. Vibrat Spectrosc 42:346–352
72. Díaz-Reyes J, Castillo-Ojeda R, Galván-Arellano M, Zaca-Moran O (2013) Characterization of WO_3 thin films grown on silicon by HFMOD. Adv Condens Matter Phys 9:591787

Publisher's Note